Qi, S & Knappett, JA 2021, 'Effect of soil permeability on soil–structure and structure–soil–structure interaction of low-rise structures', Geotechnique, pp. 1-16. https://doi.org/10.1680/jgeot.20.P.109

# Effect of soil permeability on soil-structure and structure-soil-structure interaction of low-rise structures

Qi, S. PhD[1] and Knappett, J.A. MA MEng PhD[2*]

[1] Post-doc research associate, The State Key Laboratory of Coastal and Offshore Engineering, Dalian University of Technology, Dalian, Liaoning 116024, China; (Formerly University of Dundee, Dundee, DD1 4HN, UK);

[2] Professor of Civil Engineering, University of Dundee, Dundee, DD1 4HN, UK,

[*] Corresponding author: +44-1382-384345, j.a.knappett@dundee.ac.uk

## Abstract

Earthquake-induced soil liquefaction can generate excessive damage to building structures due to significant reduction in soil effective stress. With increasing urbanisation and population growth, the performance of closely-spaced buildings, such as those in towns and cities, is of greater concern where structure-soil-structure-interaction (SSSI) may occur in conjunction with full or partial liquefaction. This study investigates the seismic performance of isolated and adjacent structures built on shallow foundations on soils of different permeability (i.e. with different amounts of drainage and therefore generating different amounts of excess pore water pressure) using a combination of dynamic centrifuge modelling and Finite Element Modelling (FEM). The results demonstrate that the reduction in free-field ground surface intensity measure (specifically, Housner Intensity) due to increasing liquefaction can be correlated to an index which is the normalised integral of excess pore pressure ratio ($r_u$) with depth. This index can express the amount of liquefaction uniquely even when full liquefaction occurs to only partial depth, or where excess pore water pressures are increased but below the level of full liquefaction at all depths. This underlying correlation means that structural demand reduction (e.g. reduction in inter-storey drift ratio) with liquefaction (SSI effect) can be linked to either (i) the $r_u$-depth index, (ii) the depth of the liquefaction front, that can be estimated from a liquefaction triggering analysis; or (iii) the

ground surface intensity amplification/attenuation in the free-field from the results of 1D free field soil column analyses. Where there are adjacent structures, a strongly beneficial SSSI effect on co-seismic settlement and detrimental effect on drift in non-liquefied soil, as observed in this and previous studies, reduced towards a null-effect in both cases with increased liquefaction, with liquefaction appearing to isolate the structures from each other (at least for the configuration considered herein). This has also been linked to the amount of amplification/attenuation of surface ground motion in the free-field (or amount of liquefaction) as a simple indicator of the likely importance of SSSI effects in liquefiable soil.

**Keywords:** Centrifuge modelling; Earthquakes; Finite-element modelling; Liquefaction; Sands

# 1. Introduction

Earthquake-induced soil liquefaction can generate excessive damage (settlement and tilting) to low-rise structures built on shallow foundations due to the significant reduction in soil effective stress. Soils with differing particle size distributions and relative densities in granular soils can see different amounts of excess pore water pressure (EPWP) rise resulting in either full or partial liquefaction, which will affect near-surface ground motions and seismic foundation bearing capacity. Previous studies have found that the behaviour of liquefiable soil beneath simple shallow foundations is different to that in free-field soil through field observation (Yoshimi and Okimatsu, 1977; Adachi et al, 1992) and experiments (Liu and Dobry, 1997; Bertalot &Brennan, 2015; Dashti et al, 2010), though analytical and numerical simulations struggle to replicate behaviours of buildings on liquefied soil accurately, and there is no widely accepted simplified method to evaluate the damage to existing foundation on different types of soil.

Liquefaction triggering analyses (Seed et al. 2003; Idriss and Boulanger 2008) can be used to assess the likelihood of soil becoming fully-liquefied, based on the peak ground acceleration (PGA) as an earthquake intensity measure (IM) and soil resistance (typically either from SPT blowcount, CPT cone resistance or shear wave velocity). However, these methods cannot be used to quantify the performance (i.e. displacements) of structures at such sites. However, recent studies have suggested that

other IM's may be more directly correlated to structural or foundation performance. One such measure, Housner intensity ($I_H$), is a typical spectra-based IM which is the integral of the pseudo-velocity spectrum over a wide period range capturing important aspects of the amplitude and frequency content (within the range of primary importance for structures; Yakut et al, 2008). $I_H$ has been suggested as an efficient predictor of the seismic response of soil deposits for both liquefiable and non-liquefiable soils by Bradley et al. (2009) and has also shown stronger correlation with structural inter-storey drift (as an engineering demand parameter, EDP) than other IMs for structures on shallow foundations in non-linear soil (Yakut et al, 2008; Cantagallo et al, 2012). Cumulative absolute velocity (*CAV*) is an alternative IM obtained by integrating the acceleration time history, incorporating intensity, frequency content, and duration of the motion into a single parameter (Karimi & Dashti, 2016). Kramer (1996) and Kramer &Mitchell, (2006) have also stated that *CAV* has shown a good correlation with structural damage. Karimi & Dashti (2016) stated that the best combination of efficiency, sufficiency, and predictability was found in *CAV* for permanent foundation settlement of shallow foundations compared to other IMs considered (including PGA, $I_H$ and Arias intensity) on liquefied soil.

Excessive settlement and angular distortion of buildings on shallow foundations has been notably observed within urban centres such as during the 2010-2011 Canterbury Earthquake Sequence (e.g. Luque and Bray, 2017). Buildings in urban areas are often closely spaced and their (coupled) dynamic response is different compared to when they are in isolation. Studies on structure-soil-structure interaction (SSSI) were initiated by Warburton et al, (1971) who extended the analytical model of soil-structure interaction proposed by Parmelee (1967) to two circular mass foundations attached to the surface of an elastic half-space and subject to periodic forces and moments. Since many influencing factors (e.g. dynamic characteristics of adjacent structures, properties of the subsoil, distance between structures and layout of structures) can contribute to SSSI, a number of analytical and numerical parametric studies have since been conducted (e.g. Lee & Wesley, 1973; Wong et al, 1975; Alexander et al, 2013; Wirgin & Brad, 1996 and Tsogka & Wirgin., 2003), but these are limited to linear elastic subgrades that are only crude representations of soil.

77 Experimental work in this field has also been conducted over the years. work by Aldaikh et al.
78 (2015, 2016) used 1-g shaking table tests to validate such modelling approaches with simple single-
79 degree-of-freedom models on a linear-elastic half space (foam) and demonstrated that structural peak
80 acceleration and spectral power can be significantly influenced either beneficially or detrimentally
81 depending on the relative dynamic properties (principally natural period) of adjacent structures. The
82 greatest SSSI effects on structural demand were observed when the natural period ratio between
83 adjacent structures was around 1.2. Work done by Knappett et al. (2015), Mason et al. (2013) and
84 Trombetta et al (2015) on non-linear soil using geotechnical centrifuge modelling also showed that
85 SSSI effects can impose potential beneficial and detrimental effects on foundation and structural
86 behaviours of adjacent buildings. Knappett et al. (2015) further demonstrated that SSSI can also
87 strongly influence the post-earthquake settlement and rotation of structures, associated with the
88 foundation behaviour. Initial work investigating SSSI effects on liquefiable soil has undertaken by
89 Hayden et al. (2015), with a generally lower structural response (in terms of spectral acceleration)
90 observed in structures. Work done by Kirkwood & Dashti (2018) found that the rotation of adjacent
91 structures depends on a combination of three systems, which may cause the adjacent structures to rotate
92 inwards to or outwards from each other. Qi & Knappett (2020) found that raft foundations can be more
93 beneficial in reducing structural demand (in terms of peak storey acceleration and inter-storey drift)
94 than separated strip foundation due to the effects of SSSI. Although the complexity has not been fully
95 understood, remediation for reducing the detrimental effects caused by SSSI has been studied including
96 the use of vertical drains, soil densification and reinforcement by ground walls (Kirkwood & Dashti,
97 2019; Olarte et al, 2017), with recommendations made according to the specific configurations of
98 adjacent structures. Among all of these efforts, the influence of soil properties, such as soil permeability,
99 was not considered in previous studies.

100 This study will therefore focus on the effect of different permeability of soils generating varying
101 EPWP on the seismic behaviour of isolated and also adjacent structures considering SSSI effects. Three
102 types of soil were considered, soil permeability $k$ ranged from infinity (fully non-liquefiable), to soil of
103 high permeability (high drainage speed) and soil of low permeability (low drainage speed). Liquefiable

soil conditions were simulated using dynamic centrifuge modelling on saturated ground. Non-liquefiable soil was simulated using comparable FEM simulations on a non-linear subgrade with a fully drained response, using an approach which has previously been validated against the non-liquefied centrifuge data of Knappett et al. (2015). EDPs of foundation response (foundation settlement and tilt) and structural response (inter-storey drift or drift ratio) of multi-degree of freedom two-storey structures with strip foundations are considered, both for isolated structures and building pairs. Correlations between observed performance and free-field IMs (specifically $I_H$ and *CAV*) are presented to identify an IM which can be derived from site response analyses to evaluate potential building damage across the range of EPWP profiles that can be generated.

# 2. CENTRIFUGE MODELLING

Four multi-event centrifuge tests (configurations shown in Table 1) were conducted at the University of Dundee, UK, using the Actidyn Systèmes C67 3.5 m radius beam centrifuge facility, at 1:40 scale and tested at 40-g. All parameters are presented at prototype scale unless otherwise stated.

*Table 1 Centrifuge test configurations*

| Test No. | Configuration | Permeability | Foundation edge-to edge spacing(m) |
|---|---|---|---|
| SQ01 | B1 (isolated) | High | N/A |
| SQ03 | B1 (isolated) | Low | N/A |
| SQ05 | B1, B2 (adjacent) | High | 1.2 |
| SQ06 | B1, B2 (adjacent) | Low | 1.2 |

## 2.1. Model structures

The prototype structure considered herein was based on an idealised two storey, single bay, steel moment resisting frame with concrete slab floors sitting on separated strip concrete foundations (structure type B1, Static vertical factor of safety $FS_v = 3$) which was representative of a typical low-rise structure in an urban/suburban area. This type of structure is most likely to be treated without detailed seismic design compared to high-value multi-storey structures in central business districts. To

study SSSI effects, a neighbouring structure on the same strip foundations (structure type B2) was considered. B2 had the same lateral stiffness in the structural frame but an increase in slab mass in both storeys (by +44%) resulting in a lengthening of the fixed-base natural period $T_n$ by +20% and an increase in the bearing pressure on the foundations ($FS_v$ = 2.5). The natural period ratio between B2 and B1 was expected to generate the greatest SSSI effects according to Aldaikh et al. (2016), based on a study of the influence of SSSI on a linear elastic subgrade.

The target fundamental natural fixed-base period of B1 was selected following Equation 1:

$$T_n = 0.1N \tag{1}$$

where $N$ is the number of stories of the structure ($N$=2 in this case). The equivalent single-degree-of-freedom stiffness of the structure in the fundamental mode ($K_{eq}$) was then determined from Equation 2:

$$T_n = 2\pi\sqrt{\frac{M_{eq}}{K_{eq}}} \tag{2}$$

where:

$$\mathrm{M_{eq}} = \mathrm{M_1}\,\overline{y_1}^{\,2} + \mathrm{M_2}\,\overline{y_2}^{\,2} \tag{3}$$

$$K_{eq} = K_1(\overline{y_1})^2 + K_2(\overline{y_2} - \overline{y_1})^2 \tag{4}$$

$M_1$ and $M_2$ are the mass of each storey slab ($M_1 = M_2$). The slab mass of B1 was calculated based on a 3.6 m × 3.6 m × 0.5 m thick reinforced concrete slab and B2 represents a thicker slab, or a 0.5 m thick slab with additional fixed equipment compared to B1. The normalised modal coordinates for B1 were $\overline{y_1}$=0.45and $\overline{y_2}$=0.89 in the fundamental mode, for storeys 1 and 2, respectively, from an eigenvector analysis. The lateral stiffness of the four columns ($k_{col}$= $0.25K_1$ = $0.25K_2$) were the same. After selecting the prototype steel Universal Column size to provide sufficient bending stiffness $EI$ (UC 203×203×86) based on the calculated value of $k_{col}$, the fixed-base natural periods of B1 and B2 were 0.21 s and 0.25 s, respectively.

The model structures were scaled down according to the centrifuge scaling laws provided in Wood (2004). The structural frames, consisting of four individual square columns were made with solid

6082-series aluminium alloy rods (storey height of 3 m at prototype scale) scaled down according to stiffness. The storey slabs of B1 and B2 were fabricated from similar aluminium plates (3.6 m × 3.6 m area at prototype scale) with thin steel plates bolted on top to provide the required floor mass and allow this to be varied. B2 had additional thin steel plates compared to B1 to achieve the mass difference and period lengthening. Dimensions of the instrumented model structures B1 and B2 are shown in Figure 1 with dimensions given at prototype scale (model scale in brackets). A thin layer of epoxy resin was used to apply a coating of sand to the foundation base and sides to provide a rough soil-footing interface similar to concrete cast in-situ. The detailed properties of the two structures are given in Table 2.

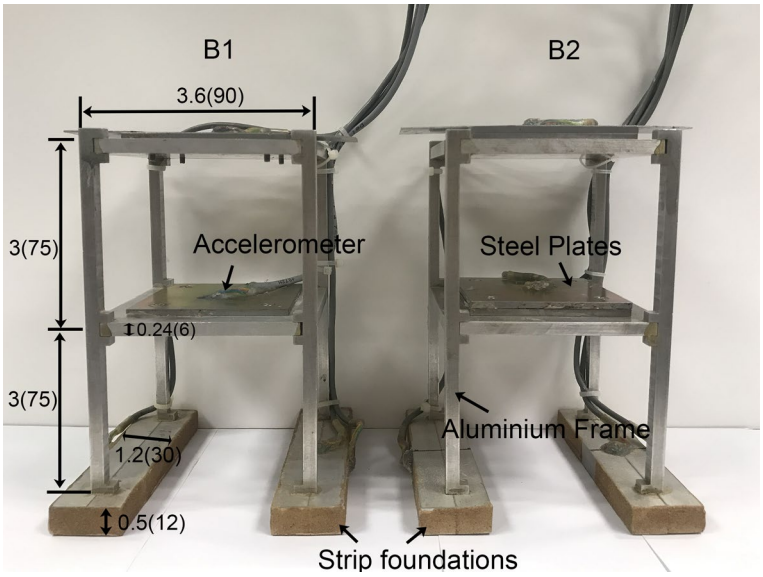


**Figure 1** Photo of model structures – Left: B1 'light' structure; Right: B2 'heavy' structure. Dimensions at prototype scale in m (model scale in mm).

*Table 2 Properties of model structures (at prototype scale)*

| Parameter | B1 (Light structure) | B2 (Heavy structure) | Units |
|---|---|---|---|
| Storey height | 3 | | m |
| Total height | 6 | | m |
| Concrete slab dimensions | 3.6×3.6×0.5 | 3.6×3.6×0.7 | m |
| Stiffness of columns, EI | 20.9 | | $MNm^2$ |
| $K_1$, $K_2$ | $37.1\times10^6$ | | N/m |
| $M_1$, $M_2$ | $16.5\times10^3$ | $23.8\times10^3$ | kg |
| Bearing pressure | 50 | 62 | kPa |
| $FS_v$ | 3 | 2.5 | - |
| Fixed-base fundamental period | 0.21 | 0.25 | s |

158

159 ## 2.2. Model preparation and soil properties

160 A soil of high permeability was achieved by saturating medium dense ($D_r$ = 55%-60%) HST95
161 Congleton silica sand (physical properties given in Table 3) with water; soil of low permeability was
162 achieved by saturating the same sand with a 40 cS hydroxyl-propyl methyl-cellulose (HPMC) solution.
163 The permeability of $D_r$ = 58% HST95 silica sand saturated with water was measured by conducting a
164 constant-head permeability test to BS 1377-5, giving $k_{low} = 1.35 \times 10^{-4}\ m/s$ representing the low
165 permeability soil (saturated with HPMC solution) at 40 g condition according to centrifuge scaling laws.
166 The high permeability soil (saturated with water) was 40 times higher, giving $k_{high} = 5.4 \times 10^{-3}\ m/s$
167 at 40g. By saturating the soil with different viscosity fluids, the two model approaches can be
168 representative of soils with permeabilities ranging from clean sand to gravelly sand according to
169 Knappett & Craig (2019), but with similar particle shape and at similar relative density. The effective
170 $D_{10}$ size of the representative soils was estimated using Hazen's Equation (Hazen 1911):

171 $$k = 10^{-2} {D_{10}}^2\ m/s \quad (5)$$

172 The calculated effective $D_{10}$ sizes were 0.12mm and 0.73mm for the low and high permeability soils,
173 respectively. These are shown in Figure 2 together with the measured particle size distribution of HST95
174 sand from Bertalot (2013) which show a close agreement for the low permeability soil. The effective
175 $D_{10}$=0.12 mm was well within the highly liquefiable zone defined by Tsuchida (1970) and the effective
176 $D_{10}$=0.73 mm was at the limit of the potentially liquefiable zone.

177 For each permeability soil, isolated and adjacent buildings tests were conducted. The layout of
178 the four centrifuge tests is shown in Figure 3. The foundation edge-to-edge spacing between the two
179 building is 1.2 m which is one third of the structure width and one quarter of the building footprint
180 (width from edge-to-edge of the foundations).

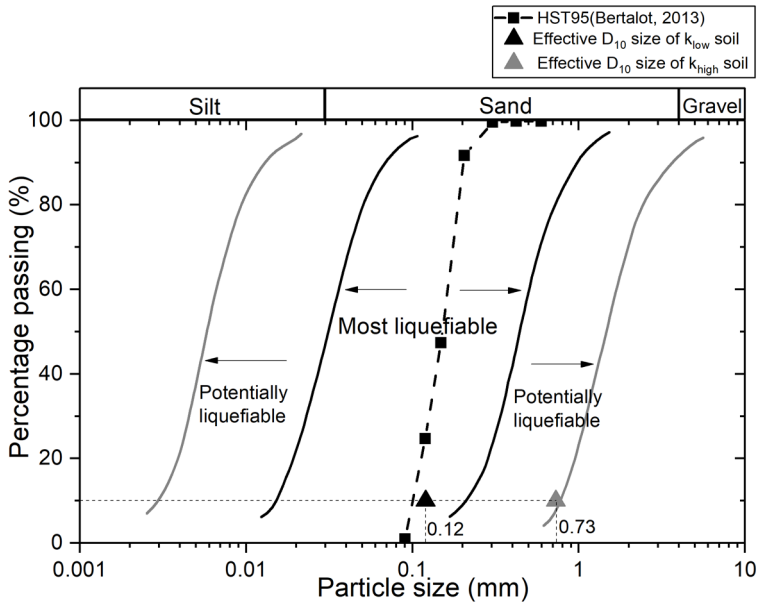


***Figure 2*** *Particle size distribution curve for HST95 sand, superimposed on liquefaction susceptibility curves from Tsuchida (1970).*

181

*Table 3 Physical properties of HST95 Congleton sand (after Lauder, 2011)*

| Property: units | Value |
|---|---|
| Specific gravity, $G_s$ | 2.63 |
| $D_{10}, D_{30}$ *and* $D_{60}$: mm | 0.09, 0.12 and 0.17 |
| $C_u$ (uniformity)and $C_z$ (curvature) | 1.9 and 1.06 |
| $e_{max}$ and $e_{min}$ | 0.769 and 0.467 |

182

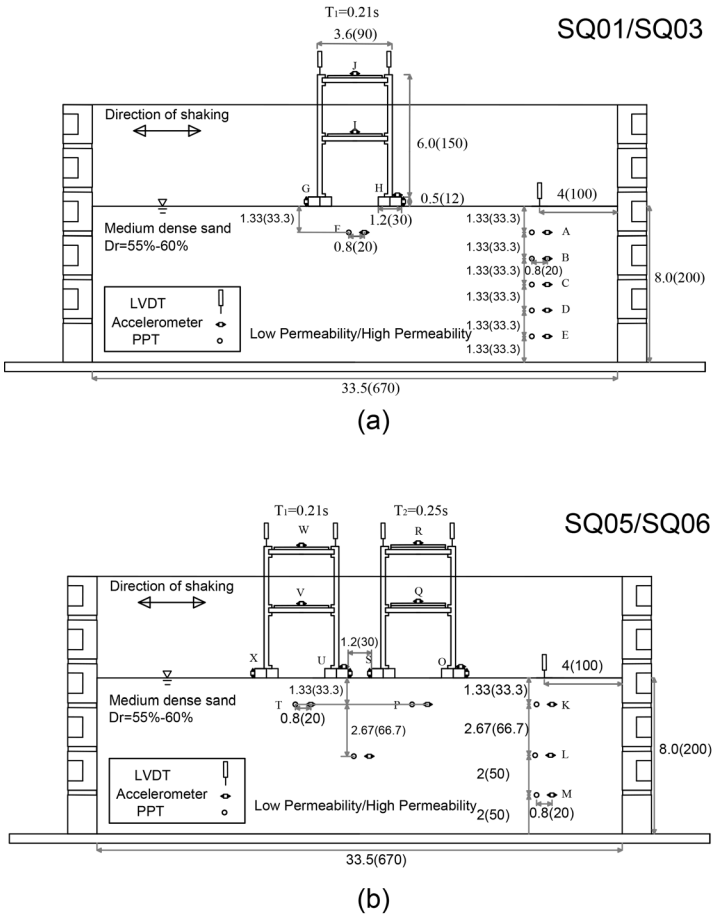


**Figure 3** Centrifuge test layout. Dimensions at prototype scale in m (model scale in mm).

The model preparation process was firstly to air-pluviate dry sand into an Equivalent Shear Beam (ESB) container to a prototype depth of 8 m. Detailed information regarding the design and performance of the ESB container can be found in Bertalot (2013). Instrumentation of the soil consisted of accelerometers (ADXL-78 single-axis MEMS devices) and pore pressure transducers (PPT; both HM-91 and PDCR-81 types manufactured by UBUT Electronic Technology and GE Sensing, respectively, were used) placed at key depths during pluviation. The instrumentation at the shallowest depth in the soil was kept at the same depth for direct comparison of the surface ground motion between isolated and adjacent tests. Isolated tests had a denser array of sensors in the free-field as fewer data acquisition channels were required for structural instrumentation. After pluviation, the soil was saturated by the pore fluid through orifices at the bottom of the ESB container under a constant gravitational head at a low flow rate until the model was fully saturated with a fluid level 2 mm at model

195 scale above the soil surface. During testing all instrumentation was sampled at 4 kHz. Due to the
196 relatively long dissipation time of EPWP in the low permeability soil (HPMC tests) after earthquake
197 events, recording was continued for 4 minutes at model scale to ensure full dissipation and
198 reconsolidation had occurred before subsequent earthquake motions were applied.

199 After saturation, the model was loaded onto the centrifuge before placing the isolated or
200 adjacent structures to minimise any disturbance of soil during loading. The model structures,
201 instrumented with horizontal and vertical accelerometers, were finally placed carefully after loading
202 onto soil surface to be as level as possible. Linear variable differential transformers (LVDT) were then
203 added to measure settlement and rotation of structures, and a further LVDT was added to record the
204 settlement of the free-field soil surface above the accelerometer/PPT array.

205 ## 2.3. Ground motions

206 The ground motions selected were a re-ordered sequence from the Canterbury Earthquake Series of
207 2010-2011 (Christchurch, New Zealand) derived from the PEER (Pacific Earthquake Engineering
208 Research) database, followed by a long duration 'double-pulse' motion from the 2011 Tohoku
209 Earthquake (Japan) derived from the National Research Institute for Earth Science and Disaster
210 Resilience. These are shown in Figure 4 in the time domain. The motions were recorded at the
211 Christchurch Botanical Gardens Station and the Ishinomaki Station, respectively. The Christchurch
212 Earthquake of February 2011 was applied initially as the principal liquefaction-inducing motion
213 ('mainshock') to generate full/near-full liquefaction in both soils. The subsequent three motions (June
214 13a Earthquake, Darfield Earthquake, June 13b Earthquake, respectively) were treated as smaller
215 'aftershocks' which could generate distinctly different distributions of EPWP rise within the different
216 soils. The final Tohoku motion was a 'double-pulse' mainshock of much longer duration which was
217 expected not only to fully re-liquefy the soil (even if densification had occurred during the preceding
218 motions), but also to apply significant seismic structural demand when the soil was fully liquefied,
219 based on previous observations that immediate strong aftershocks before significant EPWP dissipation
220 can cause continuous deformation in the ground (Okamura et al, 2001) and to a structure on already
221 liquefied soil. The use of the terms 'mainshock' and 'aftershock' are based on the strength of the motion

applied, rather than the response the motion can cause. The original motions were filtered through an eighth-order Butterworth filter with a pass range between 2.3-7.5 Hz (at prototype scale) and applied to the model using the Actidyn QS67-2 servo-hydraulic earthquake simulator (EQS) at the University of Dundee. Details of its performance may be found in Brennan et al (2014). Each successive earthquake was applied separately after the EPWP generated by the preceding motion had fully dissipated and the free-field settlement was no longer changing, as observed from the instrumentation.

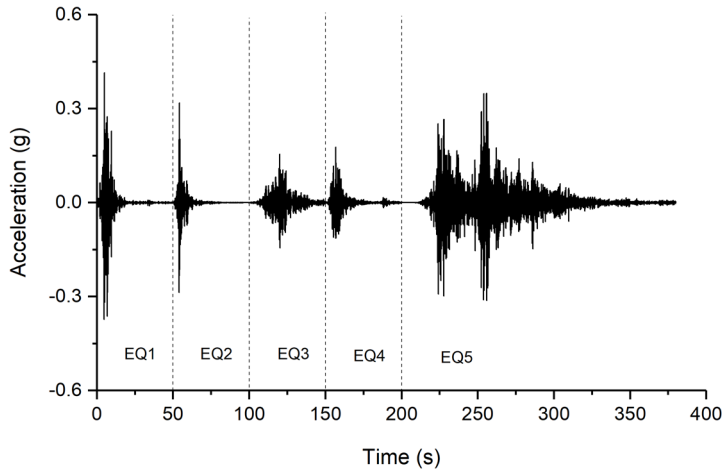


**Figure 4** Time history of input motions (full dissipation time between earthquake motions not shown).

# 3. FINITE ELEMENT MODELING (FEM)

The non-liquefiable soil cases were achieved using numerical simulation, where it was possible to achieve fully non-liquefied conditions by setting a drained response within the constitutive model. The soil and structural modelling approaches were previously validated against dynamic centrifuge testing in dry soil (drained conditions) in Knappett et al. (2015). The FEM simulations used an equivalent 2D plane strain model under uniaxial horizontal earthquake shaking, and were conducted in PLAXIS 2D 2016.

## 3.1. Structural model

The structural and foundation elements were modelled using elastic plate elements with equivalent properties per metre length which were representative of the building prototypes from Table 2. A summary of the sectional properties used is provided in Table 4. 2% Equivalent viscous damping ($\varsigma$) within the structures was simulated using Rayleigh damping (Equation 6):

$$\varsigma = c_m \left(\frac{T_n}{4\pi}\right) + c_k \left(\frac{\pi}{T_n}\right) \quad (6)$$

where mass and stiffness proportionality coefficients were set to be $c_m = 0.4$ and $c_k = 0.001$ in both structures. These values were validated against aluminium-alloy structures in centrifuge tests in (Knappett et al, 2015).

*Table 4 properties of structure in FEM*

| Prototype Properties: | Equivalent plane strain: | Units |
|---|---|---|
| Concrete Slab | $EA$=13×10$^6$ | kN/m |
| | $EI$=27×10$^4$ | kNm$^2$/m |
| | $W_{Building1}$=12.5 | kN/m/m |
| | $W_{Building2}$=18.07 | kN/m/m |
| Steel column | $EA$=4.02×10$^6$ | kN/m |
| | $EI$=11.6×10$^3$ | kNm$^2$/m |
| | $w$=9.07 | kN/m/m |
| Concrete Strip Foundations | $EA$=13×10$^6$ | kN/m |
| | $EI$=27×10$^4$ | m$^2$/m |

## 3.2. Ground profile and simulation configurations

Two FEM simulations of non-liquefiable soil were conducted using the Hardening Soil Model with Small Strain Stiffness (Schanz et al. 1999) in which the elastic behaviours was modelled using the Duncan-Chang hyperbolic stress strain model (Duncan and Chang, 1970) with non-associated deviatoric yielding via the Mohr-Coulomb criterion and a compression cap. The properties used were consistent with those previously calibrated for the Congleton HST95 sand used in the centrifuge (after Al-Defae et al., 2013). Liquefaction was prevented by specifying a dry soil model with fully drained

response and using the buoyant unit weight of the saturated ground. Utilising soil constitutive properties consistent with the centrifuge soil in a drained state ensured that the digital structural twins of the centrifuge models had the same $FS_v$ as those in the centrifuge. A simulation model with B1 in isolation, and one with B1 adjacent to B2, are shown in Figure 5. The subsoil was extended laterally to 100 m in width with non-reflecting boundary elements to avoid boundary effects (Lysmer and Kuhlemeyer, 1969). It has been shown in numerous previous studies that such boundaries provide a similar free-field response to using tied nodes (e.g. Amorosi et al, 2010 and Liang et al, 2019). A vertical depth of 8 m was simulated to be consistent with the centrifuge model. The data extracted were from the same positions as the instrumentation in the centrifuge tests. The constitutive properties used for $D_r$=55% silica sand are shown in Table 5 which match the density measured in the centrifuge tests. Additional Rayleigh damping was used to match the dynamic soil response in centrifuge tests as previously calibrated by Al-Defae et al. (2013), where $c_m$=0.0005 and $c_k$=0.005 in Equation 6 were applied.

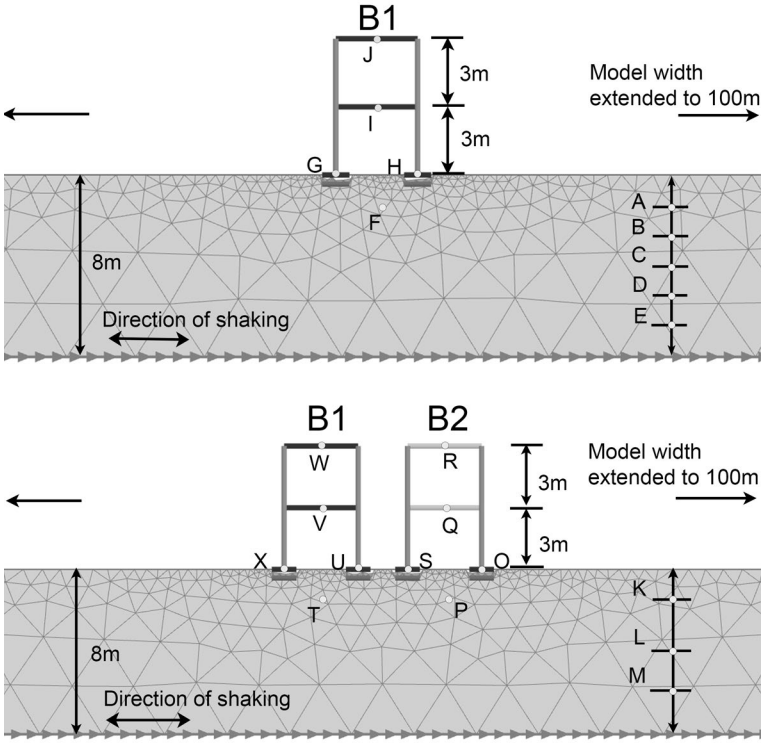


**Figure 5** FEM simulation configurations.

*Table 5 Constitutive model parameters for FEM*

| Parameter | HST95(Al-Defae et al. 2013) | Dr=0.55 | Units |
|---|---|---|---|
| $\varphi_p'$ | $20D_r+29$ | 40 | deg. |
| c' | 0 | 0 | kPa |
| $\psi'$ | $25D_r-4$ | 9.75 | deg. |
| $E_{oed}^{ref}$ | $25D_r+20.22$ | 34 | MPa |
| $E_{50}^{ref}$ | 1.25 | 42.5 | MPa |
| $E_{ur}^{ref}$ | 3 | 101.9 | MPa |
| $\nu_{ur}$ | 0.2 | 0.2 | - |
| $G_0^{ref}$ | $50D_r+88.8$ | 116.3 | MPa |
| $\varepsilon_{s,0.7}$ | $1.7D_r+0.67(\times10^{-4})$ | 1.6×10-4 | - |
| $R_f$ | 0.9 | 0.9 | - |
| m | $0.6-0.1D_r$ | 0.55 | - |
| $\gamma$ | $(1.8D_r+18.8)-9.81$ | 9.98 | $kN/m^3$ |

## 3.3. Ground motion

The input ground motion used in FEM simulations was that extracted directly from the centrifuge tests at the bottom-most accelerometer in the free-field (Points E and M in Figure 3) in the low permeability tests after scaling to prototype values. The observed variabilities from test to test were very small.

# 4. Results and discussion

This section will demonstrate the influence of soil permeability on a) site response in the free-field; b) foundation response (including foundation settlement and structural tilt) as influenced by SSI and SSSI effects, and c) structural response (peak inter-storey drift) as influenced by SSI and SSSI.

## 4.1. Site response

The maximum excess pore water pressure (EPWP) rise observed in the free-field in the liquefiable cases in each earthquake is shown in Figure 6 in terms of peak EPWP ratio $r_u$ (peak EPWP divided by initial vertical effective stress). For calculating vertical effective stress at the start of each earthquake, the positions of the PPTs in the centrifuge tests were corrected based on the static pressures measured after spin-up or any static offsets in pressure after the previous shaking to account for any floating or sinking following liquefaction and reconsolidation. Clear separation between the soils of different permeability was observed from Figure 6. Low permeability soil reached full liquefaction at all depths in EQ1 and

EQ5 (other than two slightly lower values around mid depth which may be a result of small transient sensor movements, i.e. small upwards movement, during shaking), and near the ground surface during the intervening smaller aftershocks (EQ2, 3, 4). High permeability soil reached full liquefaction to around half of the depth in EQ1, which was sufficient to influence shallow foundations, but in subsequent earthquakes, EPWP generation resulted in only a marginal reduction in effective stress at all depths, rather than full liquefaction, even in the strong final earthquake (EQ5).

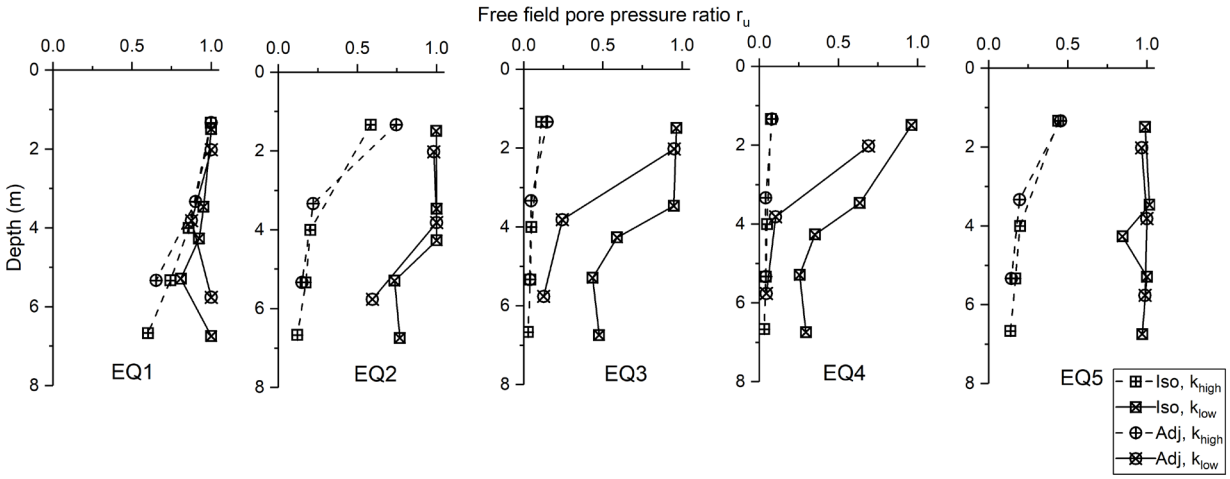


**Figure 6** Maximum amount of liquefaction observed.

The process of liquefaction generation and dissipation of the free-field mid-depth point in the isolated cases is shown in Figure 7 (EQ1, EQ2 and EQ5 are shown as examples) where maximum $r_u$ was reached at approximately the same time in the two different cases, with the maximum observed time lag across the test series being 1.4 s at prototype scale. During EQ1 (virgin soil conditions) the high and low permeability soil almost reached the same peak value, although the high permeability soil drained much more rapidly post-peak. In the subsequent motions, the high permeability soil did not reach full liquefaction conditions at the depth shown, due to soil densification and drainage. However, the peak values did still occur at approximately the same time instants.

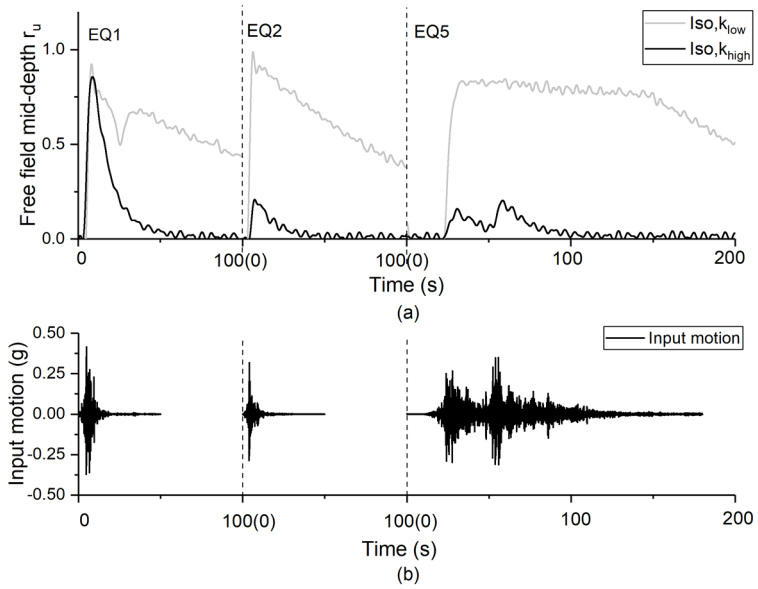


**Figure 7** (a) EPWP generation and dissipation time history with (b) input motion time history

299

300 These resulted in greater transmission of the ground motion to the free-field surface, (rather
301 than significant reduction due to shear decoupling (Wood et al, 2002) in the low permeability case) with
302 ground response more similar to non-liquefiable soil as shown in Figure 8, which shows normalised
303 response spectra for 5% nominal damping.

304 Design spectra from Eurocode 8 representing the bedrock/input (ground type A) and non-
305 liquefiable soil (ground Type E) are also shown in Figure 8 for context, as are the fixed-base natural
306 periods ($T_{B1}$ and $T_{B2}$) of the two model structures, marked with dashed vertical lines which are notably
307 on the rising/flat region of the spectra. The natural period of both structures will be lengthened in the
308 NL, $k_{high}$ and $k_{low}$ soil conditions due to SSI and soil liquefaction. The effective lengthened natural period
309 $T_n$ in the $k_{low}$ soil for the benchmark structure ($T_{B1}$) for the fundamental mode was obtained using a
310 transfer function analysis in Qi & Knappett (2020) for the five different motions (with differing amounts
311 of liquefaction) and is indicated as a range in Figure 8(d). The lengthened effective natural periods were
312 approximately double the fixed-base natural period. The ground type of low and high permeability soils
313 in which liquefaction can occur belong to ground type S2 in Eurocode 8, in which case the design
314 spectra are not directly available and require special study for the specific site. The site response changes
315 from amplification (by a factor of ~1.0-1.5 for the high permeability soil) to strong attenuation (factor

316 ~0.5-1.0) in the low permeability soil after EQ1. This verifies that, for the soil conditions considered
317 here (allowing surface drainage), soils outside of the potentially liquefiable range in Figure 2 could be
318 considered as non-liquefiable for the purposes of determination of a conservative design spectrum, even
319 if there is some (small) increase in EPWP. In the case of a NL (e.g. silty/clayey) capping layer
320 (preventing surface drainage), it is likely that a spectrum closer to lower permeability soil would be
321 more appropriate, for which using the non-liquefied spectrum may be heavily overconservative. In
322 either case, a conservative spectrum can be derived for liquefied soil.

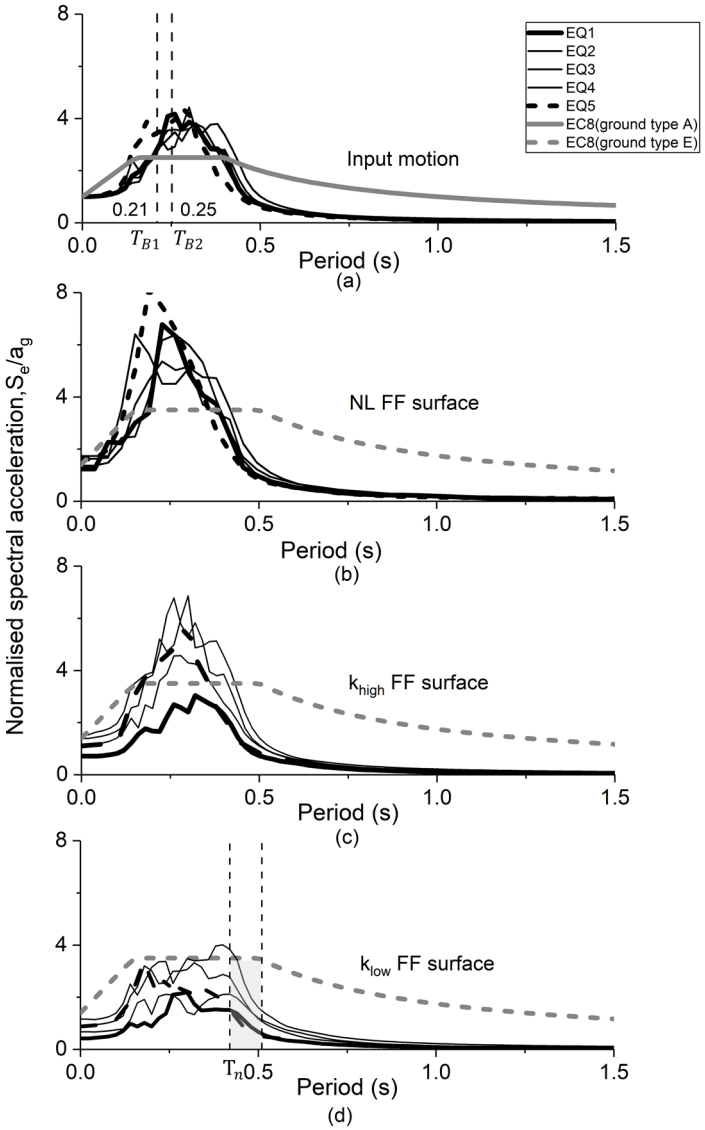


**Figure 8** Normalized response spectra for 5% nominal damping: a) input motion (bedrock); (b) free-field soil surface in non-liquefiable soil; (c) free-field soil surface in high permeability soil; (d) free-field soil surface in low permeability soil.

323

Two IMs were considered for capturing the effects of EPWP rise on the free-field site response. The first was Housner Intensity ($I_H$), derived by the integral of the pseudo spectral velocity of ground motion (spectrum with 5% nominal damping) across a period range from 0.1 to 2.5 seconds (Housner, 1952; 1963):

$$I_H = \int_{0.1}^{2.5} PSV(T, 5\%)dT \quad (6)$$

The second IM was cumulative absolute velocity ($CAV$), derived from the integral of the ground motion acceleration time history first introduced in EPRI (1998):

$$\text{CAV}=\int_0^{T_d} |a(t)|\, dt \quad (7)$$

where $T_d$ is the duration of each earthquake.

Ratios of the IM derived from the free-field surface of liquefiable soil cases divided by that of non-liquefiable soil ($I_{H,FFL}$ /$I_{H,FFNL}$ and $CAV_{FFL}$ /$CAV_{FFNL}$, respectively, which have in each case been normalised by the input IM in each test and simulations to account for any small differences between nominally identical motions) were determined. These are plotted in Figure 9 against $\left(\int_0^H r_u dz\right)/H$, a parameter representing the area beneath the $r_u$-depth curve normalised by layer depth (i.e. an index between 0-1 representing the proportion of the liquefiable layer that is fully liquefied). These ratios of IM's can be treated as a reduction factor (with a maximum value of 1) which becomes smaller as soil becomes fully liquefied over a greater depth. The relation of $I_{H,FFL}$ /$I_{H,FFNL}$ against $\left(\int_0^H r_u dz\right)/H$ ($R^2$=0.71) in Figure 9 shows a constant decreasing trend (main shocks are shaded in black and aftershocks shaded in grey). The linear correlation was:

$$I_{H,FFL}/I_{H,FFNL} = 1 - 0.5\frac{\int_0^H r_u dz}{H} \quad (8)$$

A similar linear relation was observed for $CAV_{FFL}$ /$CAV_{FFNL}$ as a function of $\left(\int_0^H r_u dz\right)/H$ ($R^2$=0.86); however, stronger correlations were subsequently observed between $I_H$ and foundation response in later analysis, so the $CAV$ correlation is not shown or utilised further.

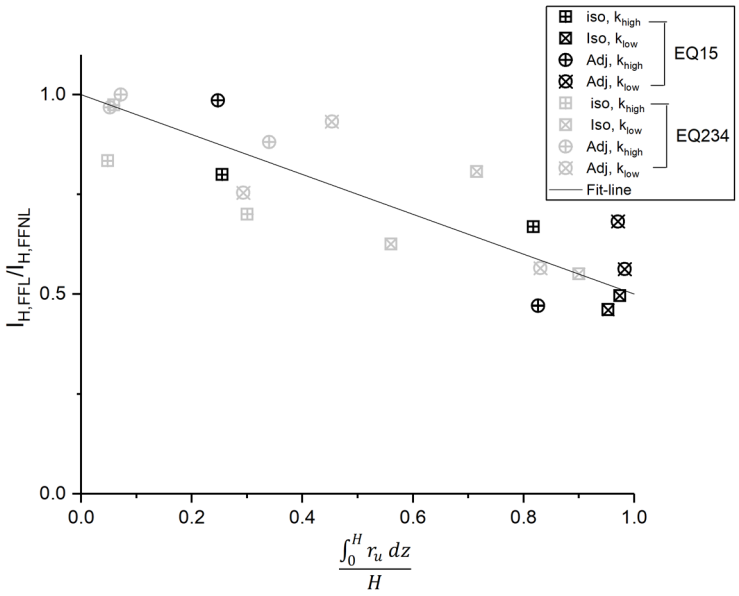


**Figure 9** Correlation of Housner Intensity changes at the free-field ground surface and input motion as a function of amount of liquefaction.

## 4.2. Foundation response

Gross co-seismic foundation settlement was derived from averaging LVDT data across each structure to remove any tilt, and final post-earthquake foundation rotation was derived from the differential settlement across the structure divided by the structures' width. The LVDT data was filtered through a low-pass zero-phase shift eighth-order Butterworth filter to provide the monotonic component with the vertical cyclic component derived from double integration and intermediate high-pass zero-phase shift filtering (also using a Butterworth filter) of vertical accelerometer data on each side of foundation. The cut-off frequencies were 0.75 Hz and 1.5 Hz at prototype scale, respectively. This method avoided the inaccuracy of individual LVDTs in recording small cyclic movements induced by shaking.

The co-seismic (gross) foundation settlement of the buildings is shown in Figure 10 (a)-(c) and can be classified by three circumstances: (1) initial co-seismic settlement caused by the first mainshock on virgin soil (with initial soil conditions fully known); (2) further smaller increments of co-seismic settlement caused by aftershocks (EQ2-EQ4); and (3) final co-seismic settlement increment caused by the highly energetic double pulse mainshock Tohoku earthquake (EQ5).

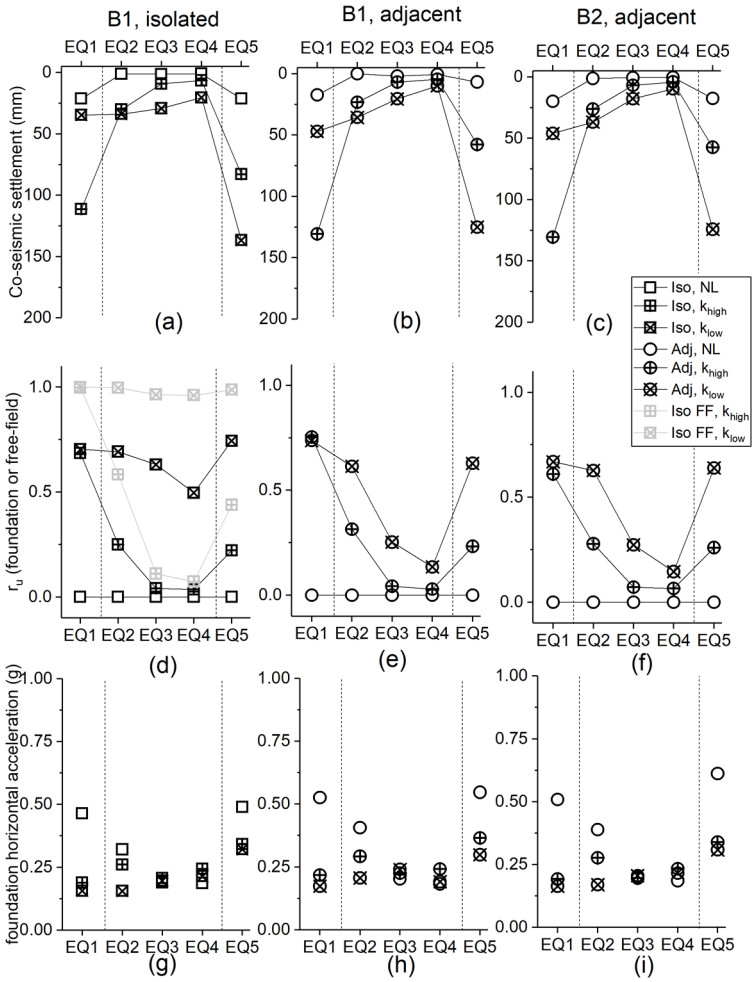


**Figure 10** (a)-(c) Co-seismic settlements for isolated and adjacent building structures; (d)-(f) peak excess pore water pressure ratio in the free-field and beneath foundations; (g)-(i) peak foundation horizontal accelerations.

362

363 For virgin soil conditions (EQ1) the co-seismic settlement induced by the initial mainshock on
364 the soil of high permeability was the greatest, larger even than that for the low permeability soil across
365 all structures. This result was attributed to the local EPWP beneath the foundations and the accelerations
366 transferred to the structure (i.e. those measured in the foundations). The $r_{u,}$ derived from beneath each
367 foundation (derived from points F, T, P in Figure 3) is shown in Figure 10 (d)-(f), along with $r_{u,}$ derived
368 from the free-field (from isolated cases) in Figure 10 (d) for comparison. The measured $r_{u,}$ beneath the
369 foundations generally follows the trend between earthquakes as exhibited in the free-field, but with
370 significantly lower magnitudes due to the additional confining stress from the foundations (which was
371 accounted for in determining vertical effective stresses, after Boussinesq), and the tendency for the soil
372 to dilate caused by additional soil strains due to the presence of the foundation. Due to the permeability

difference, the high permeability soil drained fluid more rapidly than the low permeability soil, so that the $k_{high}$ soil only reached a similar peak $r_u$ to the $k_{low}$ soil in EQ1 (in virgin soil), exhibiting much lower EPWP generation in the subsequent aftershocks.

Figure 10 (g) -(i) shows the peak horizontal acceleration transferred to the base of foundation (derived from Points H, O, U in Figure 2). In EQ1 the peak horizontal accelerations in high permeability soil was consistently 15%-20% larger than in low permeability soil. The difference in foundation input motion intensity has also been quantified via *CAV* and $I_H$ using Equations 6 and 7 (the two IMs being linked to either period or duration, rather than just peak acceleration, and should therefore have a stronger correlation with foundation co-seismic settlement than peak acceleration). The results in Table 6 demonstrate that the energy input into the structures in the low permeability case was 15%-40% lower than in the high permeability soil for both IMs. The combination of low bearing resistance ($r_u$ beneath foundation) with increased demand (foundation acceleration) resulted in greater accumulation of co-seismic settlement due to cyclic 'stamping' (e.g. similar to the mechanism described by Knappett & Madabhushi, 2008).

*Table 6 CAV of B1 and B2 during EQ1*

| | B1, isolated | | B1, adjacent | | B2, adjacent | |
|---|---|---|---|---|---|---|
| | $k_{high}$ | $k_{low}$ | $k_{high}$ | $k_{low}$ | $k_{high}$ | $k_{low}$ |
| *CAV* (m/s) | 8.13 | 5.18 | 9 | 6.96 | 8.39 | 5.55 |
| *CAV* ratio ($k_{low}$ / $k_{high}$) | 0.64 | | 0.77 | | 0.66 | |
| $I_H$ (m) | 0.27 | 0.18 | 0.28 | 0.24 | 0.25 | 0.21 |
| $I_H$ ratio ($k_{low}$ / $k_{high}$) | 0.67 | | 0.86 | | 0.85 | |

In the subsequent smaller aftershocks and the final mainshock, even with increased acceleration input into the structure(s) on high permeability soil, the local EPWP beneath the foundations was significantly reduced and dominated behaviour, resulting in much reduced co-seismic settlement increments compared to the low permeability soil case. In EQ3 and EQ4, the local EPWP in the high permeability soil was almost zero, resulting in co-seismic settlement increments for these two earthquakes which were approximately the same as the non-liquefiable case.

394 The implication of these results is that permeability appears to be very important for structures
395 on young soil deposits (e.g. reclaimed ground formed from hydraulic fill), with potentially large co-
396 seismic settlements occurring in soils of higher permeability that should be accounted for in design (i.e.
397 assuming that a strong design earthquake is the first the structure sees, e.g. EQ1 being the design
398 motion). For older deposits which have been 'shaken-down' by historical strong ground motions, larger
399 co-seismic settlements would be expected in soils of lower permeability (e.g. EQ5 is the design motion).

400 For considering the full (extended) design life of a structure, accumulated co-seismic settlement
401 as the test progressed for structure B1 was plotted against cumulative IMs ($CAV_{FF}$ and $I_{H,FF}$). The
402 strongest correlation was found with $I_{H,FF}$ and is shown in Figure 11(a). The gradients of these trendlines
403 for the three permeability soils gave $m_{NL}<m_{khigh}<m_{klow}$. It was also apparent that $m_{klow} \approx 20m_{NL}$ and $m_{khigh}$
404 $\approx 10m_{NL}$, i.e. co-seismic settlements expected for sands and gravels of different permeabilities (Figure
405 2) appear to be 1 to 1.2 orders of magnitude larger than those in non-liquefiable soil. Similar relative
406 gradient values were found for structure B2 in this study. The final points for EQ5 (at the largest $\Sigma I_{H,FF}$
407 in each test) plot above the trendlines which suggests that there may be a different rate of settlement
408 accumulation in higher intensity motions which is further explored below. The linear relationships
409 shown in Figure 11(a) are therefore not intended to be predictive equations but demonstrate the relative
410 rates of increase of settlement between the different soil conditions. If the data is replotted with the
411 motions reordered from smallest to largest intensity (not shown), these differences become more
412 apparent, but approximate fitting lines still satisfy the cumulative settlements for a given $\Sigma I_{H,FF}$ being
413 ten times higher for $k_{\text{high}}$ compared to the non-liquefied case and those for $k_{\text{low}}$ being twice those for $k_{\text{high}}$.

414 As a strong correlation was found between cumulative co-seismic settlement and $I_{H,FF}$, the
415 correlation between incremental co-seismic settlement and Houser intensity at the free field surface
416 divided by that of the input motion ($I_{H,FF}/I_{H,input}$) was attempted and is shown in Figure 11(b). The co-
417 seismic settlement caused by mainshocks (EQ1 and EQ5) are shaded in black and smaller aftershocks
418 (EQ2, EQ3 and EQ4) are shaded in grey. Mainshock points result in a steeper relationship relative to
419 the aftershocks except for two out of trendline points caused by EQ1 in the $k_{low}$ soil (due to the
420 permeability effects on virgin soil inferred from Figure 10). A clear cut-off was observed whereby co-

seismic settlement increments caused by aftershocks never exceeded those of mainshocks for the same value of $I_{H,FF}/I_{H,input}$ (which was correlated to the amount of liquefaction in Figure 9). This suggests that rather than co-seismic settlement being purely correlated to the intensity of the demand, there is possibly one of two mechanisms at play. One mechanism is a shaking history effect whereby motions that are of lower intensity than the previous historical maximum only result in small increments of settlement, with much larger co-seismic settlements observed whenever the motion is stronger than the historical maximum. The other mechanism is that there is a level of the intensity measure (e.g. $CAV$ or $I_H$) whereby motions less than that level only result in small increments, with much larger increments whenever the motion exceeds that level. IM's for the free-field ground surface for all tests can be found in Table 7 in the Appendix. $I_{H,FF}$ was inconclusive in terms of which mechanism was at play, as the values between EQ1 and EQ5 were very similar; however, $CAV_{FF}$ values indicated a much more intense motion in EQ5 compared to EQ1. To confirm which mechanism was at play, an additional motion would have been required at the end of this test series (e.g. a further EQ1 motion). However, based on El-Sekelly et al. (2016) and Dobry et al. (2015), there is evidence of the shaking history concept described above controlling free-field soil liquefaction under multiple successive ground motions, so the shaking history mechanism is more likely to also be the mechanism underpinning this data.

For a given soil permeability (e.g. comparing black cross markers with grey cross markers), the aftershocks generally exhibited higher values of $I_{H,FF}/I_{H,input}$ and lower co-seismic settlement than mainshocks due to lower EPWP generation. The general increasing trend of co-seismic settlement as IM amplification reduces explains the gradient ($m$) increasing in Figure 11(a).

In consideration of SSSI effects on co-seismic settlement, the increase in co-seismic settlement of structure B1 ($(S_{B1,adj}/S_{B1,iso})$ -1) due to the presence of adjacent structure B2 is shown in Figure 12 as a function of $I_{H,FF}/I_{H,input}$. An increasing trend from a strongly beneficial effect to a detrimental effect caused by SSSI was observed with a decrease in the IM ratio (i.e. increased amount of liquefaction and less ground motion transmission to the ground surface). A dashed line was fitted through the data points as an indication of trend (rather than a robust design equation, $R^2$ being only 0.34), indicating that the transition from beneficial to detrimental effect occurred at approximately the point where the ground

surface motion changed from amplification to attenuation (i.e. $I_{H,FF}/I_{H,input} = 1$). Non-liquefied centrifuge data from Knappett et al. (2015) was also added, for a similar case of two adjacent low-rise structures on shallow foundations, but where the structure in question ($T_n = 0.3$ s) was adjacent to a much heavier structure ($T_n = 0.6$ s). Comparing this to the non-liquefiable data from this study, it may be inferred that as an adjacent building becomes heavier, it may have an increasingly protective effect in reducing the co-seismic settlement of the lighter structure.

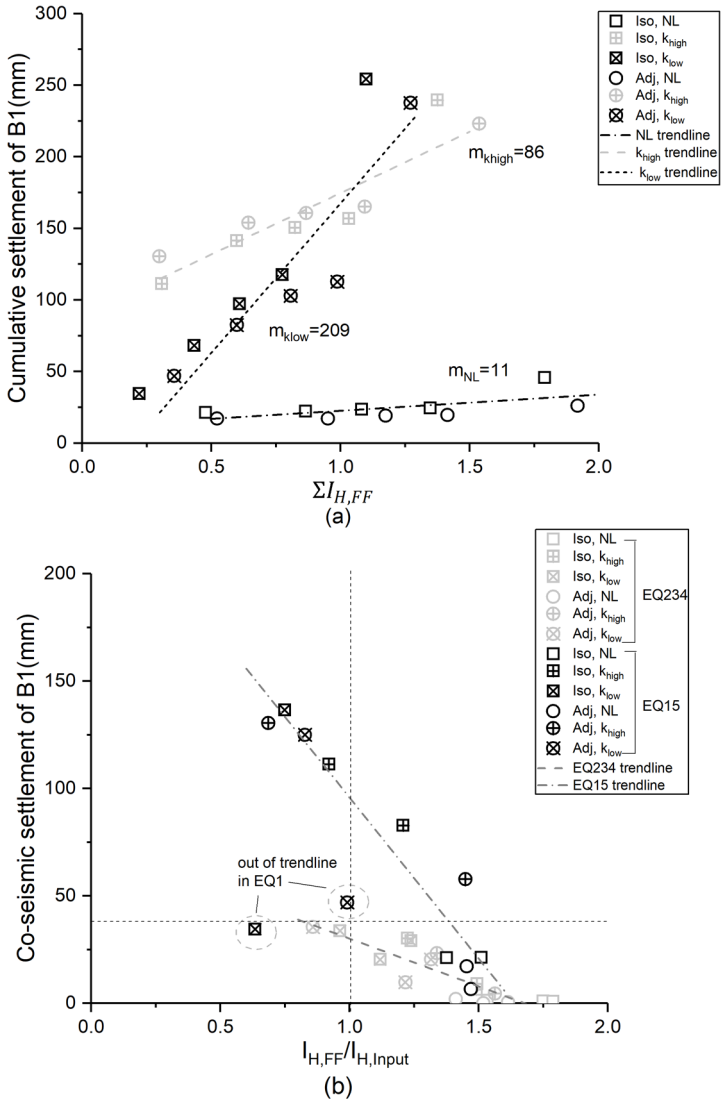


**Figure 11** (a) Correlation of accumulated settlement of structure B1 and $\Sigma I_{H,FF,}$ (b) correlation of co-seismic settlement of B1 and $I_{H,FF}/I_{H,input.}$

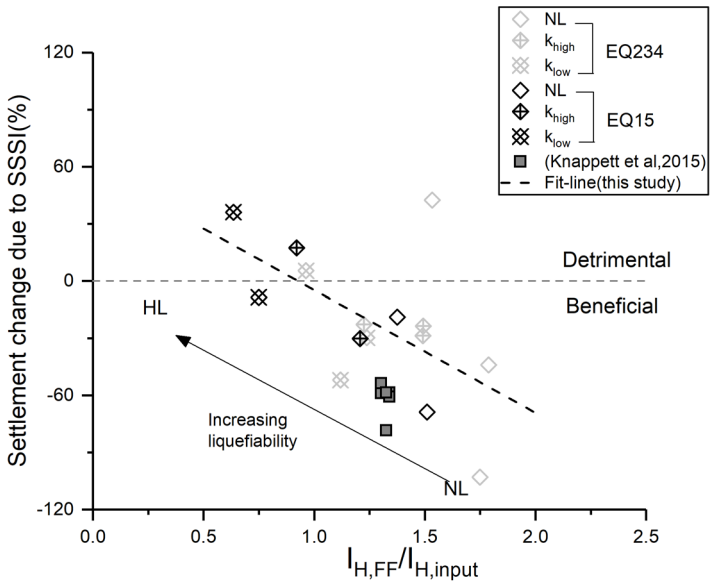


**Figure 12** Changes in co-seismic settlement increments due to SSSI.

455

456 The magnitude of rotation of the isolated building is shown in Figure 13(a). Structure B1 on
457 low permeability soil rotated the most, by approximately 0.5 degrees by the end of the earthquake
458 sequence. Rotation on high permeability soil was similar to the structure on non-liquefied soil. In the
459 adjacent cases shown in Figure 13 (b) and (c), the direction of rotation is shown as positive when
460 rotating clockwise (as shown on Figure 3). By comparing Figure 13 (a) and (b), the addition of structure
461 B2 generally increased the magnitude of rotation of B1. B1 and B2 rotated outwards from each other
462 on both high and low permeability liquefiable soil. Field observations and centrifuge tests have also
463 observed such outwards rotation of adjacent structures on shallow foundations on liquefied soil
464 (Gazetas et al, 2004; Hayden et al, 2015). For all cases, aftershocks tended to worsen the cumulative
465 rotation. The increased magnitude of rotation due to SSSI effects appeared to be more severe compared
466 with the detrimental effect on co-seismic settlement shown in Figure 12. It must be remembered that
467 rotation is a distortional measure related to differential settlements, unlike co-seismic gross settlement
468 which is an average measure. What this might suggest is that in the liquefied cases, the effect of extra
469 confinement ($r_u$ reduction) due to the adjacent building on one side of structure B1 was locally large
470 compared to the other side of B1 where there was no structure. This would amplify the rotation effect
471 due to dissimilar strength in rotating inwards or outwards from the adjacent structure. If this effect was

very localised, the average effect of increased confinement across the foundation (affecting gross settlement) may have been comparatively much smaller.

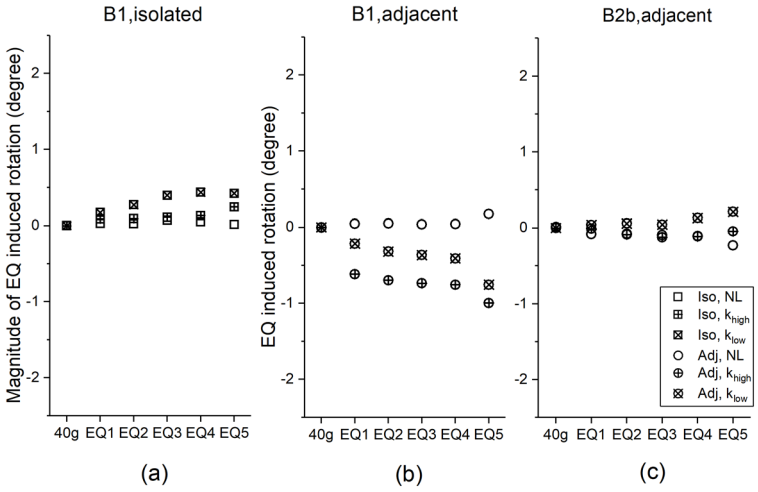


**Figure 13** (a) Magnitude of earthquake induced rotation of B1 in isolated case; (b) Earthquake induced rotation of B1 in adjacent case; (c) Earthquake induced rotation of B2 in adjacent case.

## 4.3. Structural response

The structural analysis is focussed on the first storey as this exhibited the greatest deformation and was the closest to the centre of mass of the building. Peak inter-storey drift (shown in Figure 14) is a direct measurement of distortional structural deformation, and was derived from double integration of storey acceleration data from horizontal accelerometers attached on the structures and removing the cyclic rotational (rocking) component derived from the double integral of the vertical acceleration data measured at the foundation. The acceleration data was filtered through a high pass zero-phase-shift filter (cut-off frequency 1.5 Hz at prototype scale) to remove any monotonic component due to permanent deformation before integration.

Figure 14 indicates that both soil permeabilities exhibited reduced structural demand (drift) by a significant amount such that design for non-liquefiable soil conditions can provide an upper bound for structural response. The structural benefits of the partial liquefaction observed for the high permeability cases was almost as significant as that for the low permeability cases, such that even

modest increases in EPWP (but not necessarily full liquefaction) can have a substantially protective effect, even in cases with SSSI. Similar protective effects of liquefaction were observed by Cubrinovski et al. (2019) through field observations of 50 sites from severely liquefied to non-liquefied during the Canterbury Earthquake Sequence, in which a continuous liquefiable layer was effective in increasing EPWP generation and reducing acceleration reached to the soil surface, so that the response of overlying structures can be largely reduced. Considering the protective effects on structural response alongside the foundation response discussed in Section 4.1, the effects of liquefaction can be seen as a trade-off, whereby reduced structural response comes at the expense of increased damage (settlement, rotation) to the foundation. Similar observations have been made for rocking isolation of structures, such as the bridge piers on non-liquefiable soil presented by Loli et al. (2014).

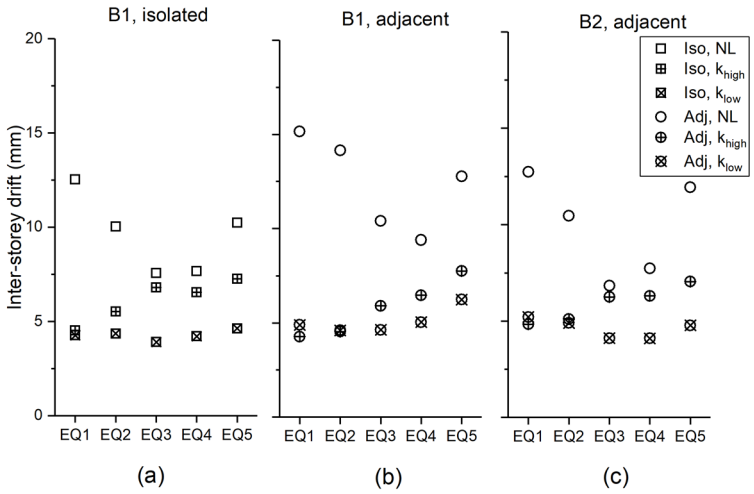


**Figure 14** (a) Inter-storey drift of structure B1 in isolated case; (b Inter-storey drift of B1 in adjacent case; (c) Inter-storey drift of B2 in adjacent case.

The ratio of inter-storey drift in the liquefied case divided by that of the non-liquefied case ($D_L/D_{NL}$) of structure B1 is plotted with $I_{H,FFL}/I_{H,FFNL}$ in Figure 15 in which correlation for isolated cases was more obvious. Potential relationships fitted through isolated and adjacent cases are shown in the figure (Equation 9 for isolated cases, and Equation 10 for adjacent cases). The fit-line of a power function in these relationships is proposed, rather than a linear function, to achieve a higher closeness

of fit while satisfying the condition of $D_L/D_{NL}$=1 (no reduction of drift) when $I_{H,FFL}/I_{H,FFNL}$=1 (no liquefaction effect).

$$D_L/D_{NL} = \left(I_{H,FFL}/I_{H,FFNL}\right)^{1.6} \quad (9)$$

$$D_L/D_{NL} = \left(I_{H,FFL}/I_{H,FFNL}\right)^{2.6} \quad (10)$$

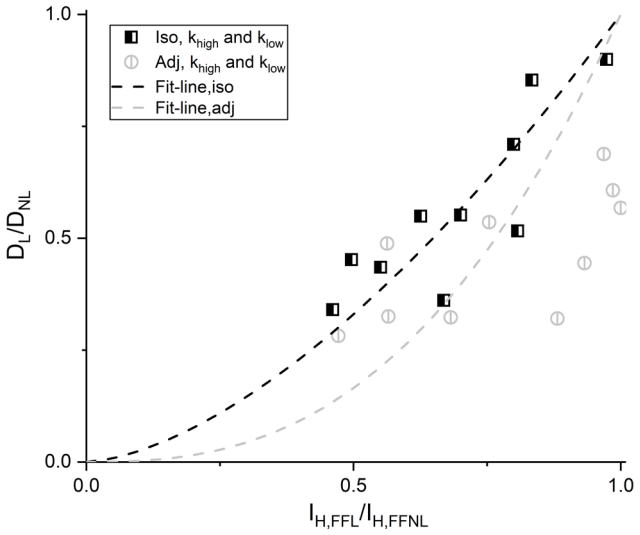


**Figure 15** Reduction of structural inter-storey drift due to liquefaction (SSI effect).

These relationships were substituted into the linear relationships in Figure 9 between $I_{H,FFL}/I_{H,FFNL}$ and $\left(\int_0^H r_u dz\right)/H$ resulting in a drift reduction factor linked to the amount of liquefaction. By assuming a simple bi-linear $r_u$ profile with depth in which the maximum EPWP values are assumed to be constant with depth below the depth of full liquefaction, the normalised depth of full liquefaction (the liquefaction front) can be linked to the value of $\left(\int_0^H r_u dz\right)/H$. Details of this method are described in the appendix. The relationship is shown in Figure 16 (a) with the proportion of full liquefaction layer over the depth of the soil linked to $H_{crit}/H$, where $H_{crit}$ is the depth of fully liquefied soil, i.e. depth of the liquefaction front (shown in the inset diagram in Figure 16(a)). The relationship was approximated as:

$$\frac{\int_0^H r_u dz}{H} = 1 - e^{-4H_{crit}/H} \quad (11)$$

By substituting Equation 8 and 11 in Equations 9 and 10 the liquefaction reduction factor on drift can be linked to the depth of full liquefaction by:

$$\left.\frac{D_L}{D_{NL}}\right|_{iso} = \left(1 - 0.5\left(1 - e^{-4H_{crit}/H}\right)\right)^{1.6} \quad (12)$$

$$\left.\frac{D_L}{D_{NL}}\right|_{adj} = \left(1 - 0.5\left(1 - e^{-4H_{crit}/H}\right)\right)^{2.6} \quad (13)$$

These relationships are shown in Figure 16(b), compared with the centrifuge/FEM data (where $H_{crit}/H$ was determined experimentally from Figure 6). It suggests that the effect of liquefaction is continuously developed with the proportion of fully liquefied layer. Both Equations (12)-(13) and the centrifuge data suggest a maximum reduction of storey drift by 60-70% once the depth of the liquefaction front is greater than approximately half the depth of the liquefiable layer, i.e. the soil does not have to be fully liquefied over the entire depth to fully observe the protective effects of liquefaction on structural demand. The effect of SSSI was seen to result in generally lower $D_L/D_{NL}$, especially when the depth of full liquefaction layer was small (i.e. in cases of partial liquefaction).

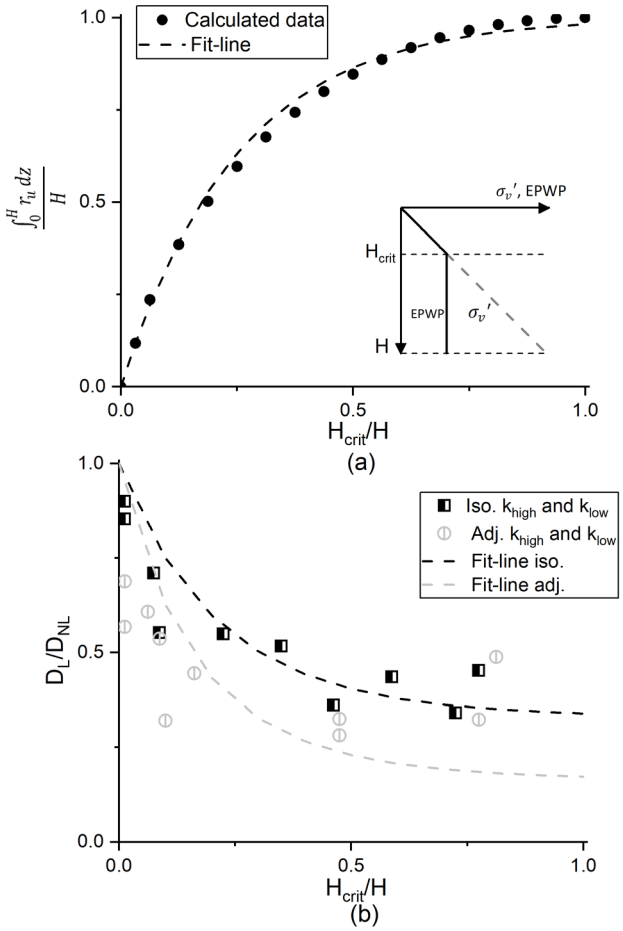


**Figure 16** (a) Relationship between index of normalised amount of liquefaction and normalised depth of the liquefaction front; (b) Reduction of structural inter-storey drift due to downwards progression of the liquefaction front.

531

532 An alternative interpretation, using foundation width ($B$) to normalise the depth of the
533 liquefaction front ($H_{crit}$), rather than the depth of soil layer ($H$), was also attempted, as building
534 dimension might also play the dominant role. The alternative relationships to Equations 12 and 13 are
535 given by Equation 14 and Equation 15, respectively:

536 $$\left.\frac{D_L}{D_{NL}}\right|_{iso} = \left(1 - 0.5\left(1 - e^{-0.6H_{crit}/B}\right)\right)^{1.6} \quad (14)$$

537 $$\left.\frac{D_L}{D_{NL}}\right|_{adj} = \left(1 - 0.5\left(1 - e^{-0.6H_{crit}/B}\right)\right)^{2.6} \quad (15)$$

538 The resulting comparison of normalisation of soil depth and foundation width are shown in Figure 17
539 (a) and (b). A limited assessment of which of the two mechanisms/normalisations may be most

appropriate has been made by applying both approaches to independently collected $D_L/D_{NL}$ data of similar isolated and adjacent structures on wider raft foundations (i.e. changing $B$ = 1.2 m for strip foundations to $B$ = 4.8 m for rafts). The inter-storey drift of these raft cases on liquefied soil ($k_{low}$) were presented in Qi & Knappett (2020) using centrifuge modelling, and non-liquefied responses were evaluated using the numerical method outlined in this paper. From this additional data, shown in Figure 17, using the width of individual foundation elements as a normalisation does not appear to result in a good fit to the data compared with using the proportion of the soil layer which is fully liquefied (i.e. Equation 12 and 13); however, it should be noted that both foundation cases considered here have the same overall footprint width (4.8 m) and that $H_{crit}/H$ = 0.6 (beyond which $D_L/D_{NL}$ becomes largely insensitive to further liquefaction) can be alternatively expressed as $H_{crit}$/footprint = 1.0. Whether the critical consideration is that the liquefaction depth has reached half the liquefiable layer depth or one building width would require additional data, varying building footprint and $H$. However, in either case, it is clear from the data presented that it is not necessary to have complete liquefaction of the entire liquefiable layer (at least where this is thicker than building footprint) for the structural demand to be fully reduced.

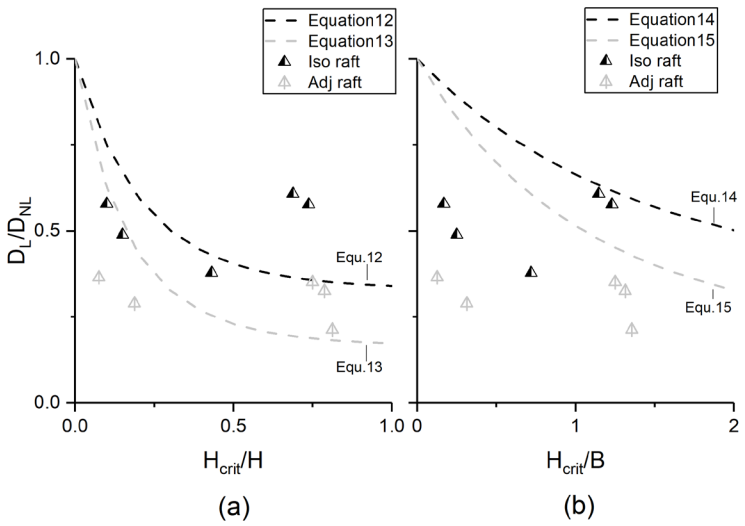


**Figure 17** Performance of alternative $D_L/D_{NL}$ correlations with (a) $H_{crit}/H$ (b) $H_{crit}/B$.

In further consideration of SSSI effects, changes to the inter-storey drift of structure B1 due to the presence of adjacent structure B2 ($D_{B1,adj}/D_{B1,iso}$ -1) is shown in Figure 18 as a function of $I_{H,FF}/I_{H,input}$. The drift values have been normalised by PGA of the input motion to remove small differences in the nominally identical input motions. In non-liquefied soil, SSSI was generally detrimental (by up to 30%) which agrees with data from Knappett et al (2015), which are also shown in Figure 18. A line was fitted to the data points in this study as an indication of trend (rather than a robust design equation, $R^2$=0.12). According to this, SSSI was seen to be generally beneficial or had little effect when liquefaction occurred to significant depth (low $I_{H,FF}/I_{H,input}$), though it appeared that the more strongly beneficial effects were observed in the higher permeability soil. For all cases, the analysis of the non-liquefiable soil condition appears to provide an upper-bound in terms of SSI and SSSI effects on structural demand. However it should be noted that only a single ratio of adjacent building natural periods ($T_{n,B2}/T_{n,B1}$ = 1.2) was considered herein, and further testing and simulation would be necessary to further generalise these results.

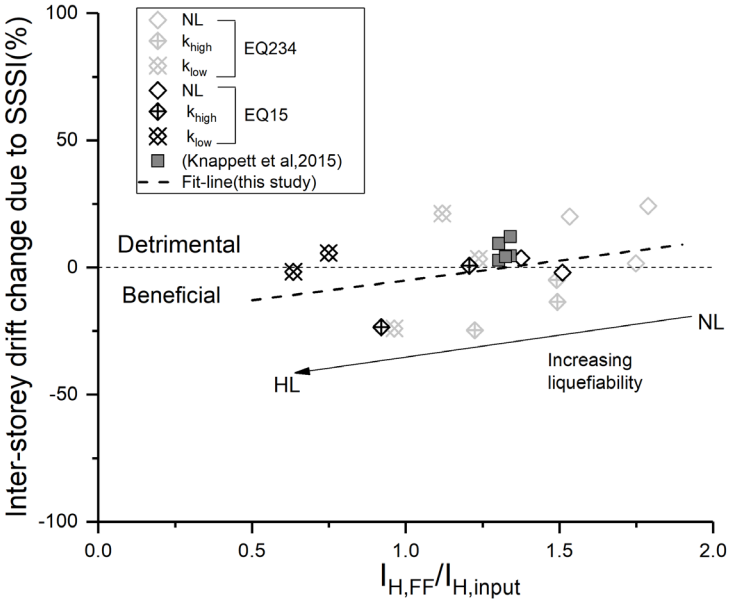


**Figure 18** Changes in inter-storey drift due to SSSI.

# 5. Conclusions

This paper has investigated the effect of soil permeability on a typical low-rise structure with separated strip foundations adjacent to a similar type of structure with a slightly longer natural period in terms of soil-structure interaction (SSI) and structure-soil-structure interaction (SSSI) effects. Soil cases of different permeabilities were considered using a combination of dynamic centrifuge modelling and Finite Element simulation. Site response, foundation response and structural response in the different soils were considered. Key points were concluded as follows:

- In the free-field, the reduction in ground surface intensity measures (IMs) with increasing amounts of liquefaction can be linearly correlated to the proportion of the soil layer which is fully liquefied through an index which is the normalised integral of $r_u$ with depth. Of the two IMs tested, both Housner Intensity ($I_{H,FF}$) and cumulative absolute velocity ($CAV_{FF}$) showed strong correlations, though $CAV$ was marginally stronger.
- Structures on young soil deposits (e.g. reclaimed ground formed from hydraulic fill) which have not seen previous strong shaking may be sensitive to permeability of the soil, with larger co-seismic settlement in soils of higher permeability in the first mainshock. For structures on older deposits which have been 'shaken-down' by historical strong motions, larger co-seismic settlements would be expected in soils that are of lower permeability (i.e. likely to see greater EPWP generation).
- Cumulative co-seismic settlements in an earthquake sequence correlate linearly with $\Sigma I_{H,FF}$ and the settlements expected for soils of different permeabilities are 1 to 1.2 orders of magnitude larger than those of non-liquefiable soil and can differ by a factor of 2 depending on permeability.
- Correlation of co-seismic building settlement increments with $I_{H,FF}/I_{H,input}$ (i.e. amplification/attenuation in $I_H$) suggests that settlement is not only correlated with

596 earthquake intensity, but also influenced by other mechanisms of either shaking history
597 or threshold intensity, which requires further study to confirm.
598 • The reduction in inter-storey drift as a function of the amount of liquefaction (SSI effect)
599 can be correlated to the amount of soil which is fully liquefied in terms of the depth of
600 the liquefaction front. The depth of the liquefaction front can be estimated by
601 liquefaction triggering analyses, suggesting that these can quantitively provide an
602 estimate of the effect of liquefaction on structural demand. The maximum reduction in
603 drift to between 30-40% of the non-liquefied value was achieved once the maximum
604 depth of full liquefaction reached approximately 50% of the layer thickness or 100%
605 of the overall foundation footprint.
606 • In terms of SSSI effects, for co-seismic settlement, a trend from a strongly beneficial
607 effect when non-liquefied (as observed in previous studies) to a null/marginally
608 detrimental effect with increased liquefaction was observed. This was accompanied by
609 a reduction in inter-storey drift from a detrimental (up to +30%) to a null/marginally
610 beneficial effect with increased liquefaction. Therefore for these two engineering
611 demand parameters, liquefaction would appear to isolate adjacent structures from each
612 other such that they exhibit the effects of SSI (increased co-seismic settlement and
613 reduced drift due to liquefaction), but not SSSI, based on the data presented here.
614 • Given the linear correlation between the amount of liquefaction and IM
615 amplification/attenuation previously noted, in broad terms, the SSSI effects of co-
616 seismic settlement reduction and drift amplification mentioned above occur for cases
617 where $I_{H,FF}/I_{H,input} > 1$ (amplification at the ground surface; non-liquefied cases and
618 partially liquefied soils), but are absent when $I_{H,FF}$ is attenuated as a result of strong to
619 full liquefaction. $I_{H,FF}/I_{H,input}$, which could be determined from 1D site response analyses,
620 may therefore be a useful indicator as to whether SSSI effects are likely to be important
621 for a group of adjacent structures on potentially liquefiable soil.

- Buildings on low permeability soil permanently rotated the most when in isolation and SSSI generally resulted in an increase in the magnitude of rotation in all non-/partially-/fully-liquefied conditions. Adjacent buildings rotated outwards from each other in liquefied soil which agrees with previous field observations.

# 6. Acknowledgements

The authors would like to thank China Scholarship Council for its financial support of the first author during her PhD studies. The authors would also like to thank Mark Truswell, Grant Kydd, Willie Henderson and Gary Callon at the University of Dundee for their assistance in fabricating the model structures and running the centrifuge tests.

# 7. Appendix

## 7.1. Intensity measure

The intensity measure of *PGA*, $I_H$ and *CAV* in the isolated cases at free-field surface (as a best description of free-field condition) are provided in Table 7.

*Table 7 intensity measure derived at free-field surface from isolated cases*

| | $PGA_{FF}$ (g) | | | $I_{H,FF}$ (m) | | | $CAV_{FF}$ (m/s) | | |
|---|---|---|---|---|---|---|---|---|---|
| Motion | NL | $k_{high}$ | $k_{low}$ | NL | $k_{high}$ | $k_{low}$ | NL | $k_{high}$ | $k_{low}$ |
| EQ1 | 0.52 | 0.31 | 0.17 | 0.48 | 0.31 | 0.22 | 16.04 | 7.66 | 4.09 |
| EQ2 | 0.47 | 0.37 | 0.18 | 0.39 | 0.29 | 0.21 | 11.01 | 6.85 | 3.31 |
| EQ3 | 0.26 | 0.25 | 0.19 | 0.22 | 0.23 | 0.18 | 12.94 | 11.20 | 7.09 |
| EQ4 | 0.26 | 0.26 | 0.18 | 0.26 | 0.21 | 0.17 | 10.24 | 8.29 | 5.50 |
| EQ5 | 0.60 | 0.40 | 0.32 | 0.44 | 0.32 | 0.22 | 80.57 | 63.91 | 12.38 |

## 7.2. Approximate method for determining $H_{crit}$ and $\left(\int_0^H r_u dz\right)/H$

This method was originally presented in Qi and Knappett (2020). The liquefaction triggering analysis was first conducted followed general accepted method in (Idriss and Boulanger,2010), in which a factor of safety against liquefaction can be determined using Equation 16.

$$F_{sL} = \frac{CRR}{CSR} \tag{16}$$

where *CRR* = Cyclic Resistance Ratio and *CSR* = Cyclic Stress Ratio. *CRR* values were estimated using equivalent normalised SPT blowcounts $(N_1)_{60}$ approximated using Equation 17 (Skempton, 1986):

$$(N_1)_{60}/{D_r}^2 \approx 60 \tag{17}$$

In which $D_r = 60\%$ gives an estimated $(N_1)_{60}$ of 22.

The *CSR* values were derived based on the *PGA* of input motion and assuming an amplification factor of 1.4 at the soil surface, this being the value recommended for ground type E in EC8 (excluding any effects of liquefaction). The $F_{sL}$ results are shown in Figure 19 as cross markers.

The distribution of $r_u$ with depth is then estimated using methods described in (Madabhushi et al, 2010), by assuming full liquefaction exists at all depths where $F_{sL} \leqslant 1$, so peak EPWP equals to effective stress at this depth; At the depth where $F_{sL}$ becomes greater than 1, the peak EPWP is assumed not change with depth anymore, while effective stress increases. $H_{crit}$ is the limiting depth when $F_{sL} = 1$. In smaller aftershocks where full liquefaction exists at a limited depth, the profile of maximum $r_u$ with depth can be determined, from which $\left(\int_0^H r_u dz\right)/H$ can be found. Examples of this method, as applied to EQ3 and EQ4 in the current study are shown in Figure 19 in which the predicted method can be seen to provide a reasonable upper-bound to the peak $r_u$ observed in the free-field.

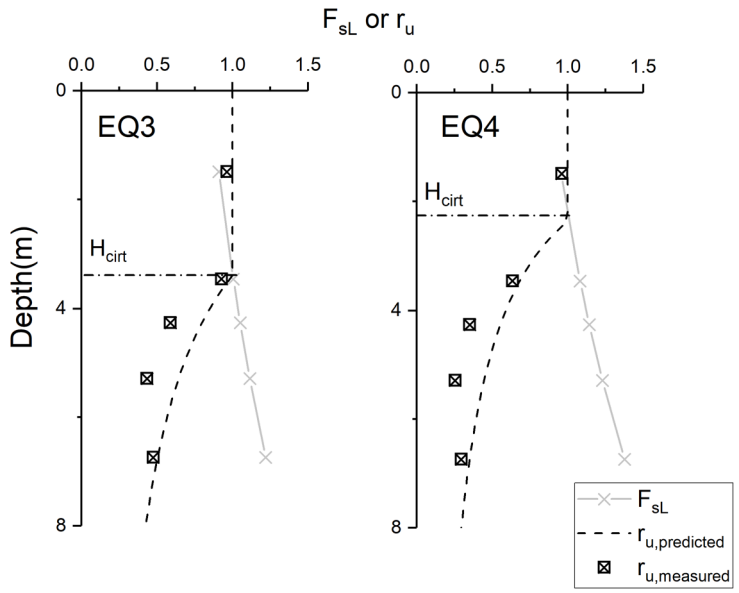


**Figure 19** derivation of $H_{crit}$

659

660

# 661 8. References


662 Adachi, T., Iwai, S., Yasui, M. and Sato, Y. (1992). "Settlement and Inclination of Reinforced-
663 Concrete Buildings in Dagupan-City due to Liquefaction during the 1990 Philippine Earthquake."
664 Proceedings of the 10th World Conference on Earthquake Engineering, 1, 147-152.

665 Aldaikh, H., Alexander, N.A., Ibraim, E. and Knappett, J. A. (2016). "Shake table testing of the
666 dynamic interaction between two and three adjacent buildings (SSSI)." Soil Dynamics and Earthquake
667 Engineering, 89:219–232.

668 Aldaikh, H., Alexander, N.A., Ibraim, E. and Oddbjornsson, O. (2015). "Two dimensional
669 numerical and experimental models for the study of structure–soil–structure interaction involving three
670 buildings." Computers and Structures. 150, 79–91.

671 Al-Defae, A. H., Caucis, K. and Knappett, J. A. (2013). "Aftershocks and the whole-life seismic
672 performance of granular slopes." Géotechnique, 63(14), 1230–1244.

673 Alexander, N. A., Ibraim, E. and Aldaikh, H. (2013). “A simple discrete model for interaction
674 of adjacent buildings during earthquakes.” Computers and Structures. 124, 1–10.

675 Amorosi, A., Boldini, D. and Elia, G. (2010). “Parametric study on seismic ground response by
676 finite element modelling.” Comput. Geotech. 37(4), 515–528.

677 Bertalot, D. (2013). “Foundations on layered liquefiable soils.” PhD thesis, University of
678 Dundee, Dundee, UK.

679 Bertalot, D. and Brennan, A. J. (2015). “Foundations Influence of initial stress distribution on
680 liquefaction-induced settlement of shallow foundations.” Géotechnique, 65(5), 418-428.

681 Bradley, B. A., Cubrinovski, M., Dhakal, R. P., MacRae, G. A., (2009). “Intensity measures
682 for the seismic response of pile foundations.” Soil Dynamics and Earthquake Engineering, 29, 1046-
683 1058.

684 Brennan, A. J., Knappett, J. A., Bertalot, D., Loli, M., Anastasopoulos, I. and Brown, M. J.
685 (2014). “Dynamic centrifuge modelling facilities at the University of Dundee and their application to
686 studying seismic case histories.” Proceedings of the 8th international conference on physical modelling
687 in geotechnics, London, UK.

688 Cantagallo, C., Camata, G., Spacone, E., Corotis, R. (2012). “Seismic demand uncertainty
689 provided by ground motion intensity measure.” 15th World Conference on Earthquake Engineering
690 (15WCEE), Lisbon.

691 Cubrinovski, M., Rhodes, A., Ntritsos, N., and Van Ballegooy, S. (2019). “System response of
692 liquefiable deposits.” Soil Dynamics and Earthquake Engineering, 124, 212-229.

693 Dashti, S., Bray, J.D., Pestana, J.M., Riemer, M., and Wilson, D. (2010). “Mechanisms of
694 Seismically Induced Settlement of Buildings with Shallow Foundations on Liquefiable Soil.” Journal
695 of Geotechnical and Geoenvironmental Engineering. ASCE. 136(1), 151–164.

Dobry, R., Abdoun, T., Stokoe, K. H., II., Moss, R. E. S., Hatton, M., and El Ganainy, H. (2015). "Liquefaction potential of recent fills versus natural sands located in high seismicity regions using shear wave velocity." Journal of Geotechnical and Geoenvironmental Engineering. ASCE. 141(3), 04014112.

Duncan, J.M. and Chang, C.Y. (1970). "Nonlinear analysis of stress and strain in soil." ASCE Journal of the Soil Mechanics and foundations Division, 96 (5), 1629-1653.

Electrical Power Research Institute (EPRI). (1998). "A criterion for determining exceedence of the operating basis earthquake." EPRI NP- 5930, EPRI, Palo Alto, Calif.

El-Sekelly, W., Abdoun, T., and Dobry, R. (2016) "Liquefaction resistance of a silty sand deposit subjected to preshaking followed by extensive liquefaction." Journal of Geotechnical Engineering and Geoenvironmental Engineering, 142(4), 04015101.

Gazetas, G.; Apostolou, M.; and Anastasopoulos, J., (2004). "Seismic Bearing Capacity Failure and Overturning of 'Terveler' Building in Adapazari, 1999." International Conference on Case Histories in Geotechnical Engineering, 8, New York.

Hayden, C.P., Zupan, J.D., Bray, J.D., Almond, J.D., and Kutter, B.L. (2015). "Centrifuge tests of adjacent mat-supported buildings affected by liquefaction. Journal of Geotechnical and Geoenvironmental Engineering 141, No. 3.

Hazen, A. (1911). "Discussion of 'Dams on sand formations,' by A.C. Koenig." Transactions of the American Society of Civil Engineers, 73, 199–203.

Housner, G.W. (1952) "Spectrum intensities of strong-motion earthquakes." Proceedings of the Symposium on Earthquake and Blast Effects on Structures. Los Angeles, California

Housner, G. W. (1963). "The behaviour of inverted pendulum structures during earthquakes." Bulletin of the Seismological Society of America, 53(2), 403–417.

Idriss, I. M. and Boulanger R. W., (2008). "Soil Liquefaction During Earthquakes." Earthquake Engineering Research Institute, USA.

720 Karimi, Z., Dashi S., (2016). “Effects of Ground Motion Intensity Measures on Liquefaction
721 Triggering and Settlement near Structures.” 1st International Conference on Natural Hazards &
722 Infrastructure (CONHIC2016). Chania, Greece.

723 Kirkwood, P. and Dashti, S. (2018). “A centrifuge study of seismic structure-soil-structure
724 interaction on liquefiable ground and implications for design in dense urban areas.” Earthquake Spectra,
725 34 (3), 1113-1134.

726 Kirkwood, P. and Dashti, S. (2019). “Influence of prefabricated vertical drains on the seismic
727 performance of similar neighbouring structures founded on liquefiable deposits.” Géotechnique, 69(11),
728 971-985

729 Knappett, J. A. and Craig, R. F., (2019). “Craig's soil mechanics.” 9th ed. CRC Press.

730 Knappett J.A. and Madabhushi, S.P.G. (2008). “Mechanism of pile group settlement in
731 liquefiable soils.” Geotechnical Earthquake Engineering and Soil Dynamics IV, Sacramento, USA,
732 May 2008, Geotechnical Special Publication No. 181, ASCE.

733 Knappett, J. A., Madden, P. and Caucis, K. (2015). “Seismic structure–soil–structure
734 interaction between pairs of adjacent building structures.” Géotechnique, 65(5), 429–441.

735 Kramer, S. L. (1996). “Geotechnical earthquake engineering.” Prentice Hall, Upper Saddle
736 River, New Jersey.

737 Kramer, S. L., and Mitchell, R. A., (2006). “Ground Motion Intensity Measures for
738 Liquefaction Hazard Evaluation.” Earthquake Spectra, Earthquake Engineering Research Institute, 22
739 (2), 413–438.

740 Lauder, K. (2011). “The performance of pipeline ploughs.” PhD thesis, University of Dundee,
741 Dundee, UK

742 Lee, T. H. and Wesley, D. A. (1973). “Considering through-soil coupling between adjacent
743 structures.” Nuclear Engineering and Design, 24(3), 374–387.

744 Liang, T., Knappett, J.A., Leung, A.K. and Bengough, A.G. (2019). “Modelling the seismic
745 performance of root-reinforced slopes using the finite-element method.” Géotechnique. 1-17.

746 Liu, L. and Dobry, R., (1997). “Seismic response of shallow foundation on liquefiable sand.”
747 Journal of Geotechnical and Geoenvironmental Engineering, ASCE, 123(6), 557-567.

748 Loli, M., Knappett, J. A., Brown, M. J., Anastasopoulos, I., and Gazetas, G. (2014). “Centrifuge
749 modelling of rocking-isolated inelastic RC bridge piers.” Earthquake Engineering and Structural
750 Dynamics, 43(15), 2341-2359.

751 Luque, R., Bray, J. (2017). “Dynamic analyses of two buildings founded on liquefiable soils
752 during the Canterbury earthquake sequence.” Journal of Geotechnical and Geoenvironmental
753 Engineering. ASCE, 143(9): 04017067

754 Lysmer, J. and Kuhlemeyer, R. L. (1969). “Finite dynamic model for infinite media.” Journal
755 of the Engineering Mechanics Division, 95(4), 859–878.

756 Madabhushi, G., Knappett, J., and Haigh, S. (2010). “Design of pile foundations in liquefiable
757 soils.” Imperial College Press.

758 Mason, H.B.,Trombetta, N.W., Chen, Z., Bray, J.D., Hutchinson, T.C., and Kutter, B.L. (2013).
759 “Seismic soil-foundation-structure interaction observed in geotechnical centrifuge experiments.” Soil
760 Dynamics and Earthquake Engineering. 48(1), 162–174.

761 Okamura, M., Abdoun, T. H., Dobry, R., Sharp, M. K. and Taboada, V. M. (2001). “Effects of
762 sand permeability and weak aftershocks on earthquake-induced lateral spreading”. Soils and
763 foundations. Japanese Geotechnical Society 41(6) 63-77.

764 Olarte, J., Paramasivam, B., Dashti, S., Liel, A., and Zannin, J. (2017). “Centrifuge modelling
765 of mitigation-soil-foundation-structure interaction on liquefiable ground.” Soil Dynamics and
766 Earthquake Engineering. 97, 304-323.

767 Parmelee, R.A.(1967) “Building–foundation interaction effects.” Journal of the Engineering
768 Mechanics Division. ASCE, 93(EM2),131–52.

769 Qi, S. and Knappett, J.A. (2020). “Influence of foundation type on seismic response of low-rise
770 structures in liquefiable soil.” Soil Dynamics and Earthquake Engineering. 128, 105786.

771 Seed, R.B., Cetin, K. O., Moss, R. E. S., Kammerer, A. M., Wu, J., Pestana, J. M., Riemer, M.
772 F., Sancio, R. B., Bray, J. D., Kayen, R. E., and Faris, A., (2003). “Recent advances in soil liquefaction
773 engineering: a unified and consistent framework.” 26th Annual ASCE Los Angeles Geotechnical
774 Spring Seminar, ASCE, USA.

775 Schanz, T., Vermeer, P. A., and Bonnier, P.G. (1999). “The hardening soil model: formulation
776 and verification.” Beyond 2000 in computational geotechnics, 281-296.

777 Skempton, A.W. (1986). “Standard penetration test procedures and the effects in sands of
778 overburden pressure, relative density, particle size, ageing and overconsolidation.” Géotechnique, 36(3),
779 425–447.

780 Trombetta, N. W., Mason, H. B., Hutchinson, T. C., Zupan, J. D., Bray, J.D. and Kutter, B.L.
781 (2015). “Nonlinear soil-foundation-structure and structure-soil-structure interaction: engineering
782 demands.” Journal of Structural Engineering, 141(7), 04014177.

783 Tsogka, C. and Wirgin, A. (2003). “Simulation of seismic response in an idealized city.” Soil
784 Dynamics and Earthquake Engineering. 23(5), 391–402.

785 Tsuchida, H. (1970). “Prediction and countermeasure against the liquefaction in sand deposits.”
786 Abstracts of Seminars in the Port and Harbours Research Institute. 3.10–3.33.

787 Warburton, G. B., Richardson, J. D. and Webster, J. J. (1971). “Forced vibrations of two masses
788 on an elastic half space.” Journal of Applied Mechanics, 38(1),148-156.

789 Wirgin, A., Bard, P-Y. (1996). “Effects of buildings on the duration and amplitude of ground
790 motion in Mexico City.” Bulletin of the Seismological Society of America, 86(3), 914-920.

791 Wong, H. L. and Trifunac, M. D. (1975). “Two-dimensional, antiplane, building-soil-building
792 interaction for two or more buildings and for incident plane SH waves.” Bulletin of the Seismological
793 Society of America, 65(6), 1863–1885.

794 Wood, D.M. (2004). “Geotechnical modelling.” London, UK: Spon Press, Taylor and Francis.

795 Wood, D. M., Crewe, A., and Taylor, C. (2002). “Shaking table testing of geotechnical models.”
796 International Journal of Physical Modelling in Geotechnics, 2(1), 01-13.

797 Yakut, A., Yilmaz, H. (2008). “Correlation of Deformation Demands with Ground Motion
798 Intensity.” Journal of Structural Engineering. ASCE. 134(12),1818-1828.

799 Yoshimi, Y. and Tokimatsu, K. (1977). “Settlement of buildings on saturated sands during
800 earthquakes.” Soils and Foundations, 17(1), 23-28.